Robust Control Architecture For Waste Heat Harvesting With Non-Inverting Buck-Boost Converter

Dario Gandini, Pierpaolo Sorbellini, Marcello Chiaberge
DET POLITECNICO DI TORINO
Corso Duca degli Abruzzi, 24, 10129
Turin, Italy
Email: Dario.Gandini@polito.it

Keywords

≪Four-switch Buck-Boost Converter (FSBB)≫, ≪Thermo-electric energy≫, ≪MPPT≫, ≪DSP≫, ≪Robust control≫

Abstract

Thermoelectric generators (TEG) can be used to harvest wasted heat. TEGs are characterized by a wide output voltage range and a considerable output resistance leading to a maximum power point dependent on the working temperature. Non-Inverting Buck-Boost converter is used to manage, from one side, the wide voltage range, and from the other a battery. This article investigates a robust control architecture to recover the maximum energy from the exhaust's heat avoiding instability issues and maximizing converter efficiency.

Introduction

A Thermoelectric generator (TEG) allows to convert electrical power from a thermal power source and thus recycle the wasted power of another working system. TEGs present power characteristics that are parabola-shaped with a maximum in which their load is equal to the internal resistance for that particular input difference of temperature and in which the output voltage of the generator is equal to their open-circuit voltage [1, 2, 3]. The converter is designed to sustain the maximum power that these generators can typically deliver in an automotive application, which is usually in the order of a few hundred watts when the maximum difference of temperature occurs [4, 5, 6]. A DC-DC converter is used to convert the electrical power from the TEG and deliver it to a battery. In [7] is presented a multilevel converter to extract power from a TEG with high efficiency; however, such architecture is space consuming and not ideal to be integrated into a vehicle. [8, 9] Use a boost followed by a buck stage with coupled inductors where the MPPT is applied to the output of the TEG both using some compensator and using the minimum function to establish a smooth transition between MPPT mode and constant current or voltage modes; [11] uses a decoupled boost plus buck converter where the maximum power point tracking (MPPT) always applied on the output power of the TEG can be used as a reference for the second buck stage; [12] using the same decoupled structure employs an MPPT algorithm on the output of the TEG to control the boost stage while a buck stage regulates the output current for a battery. Here a non-inverting buck-boost topology is used, reducing the number of inductors while still allowing the harvesting with input voltages lower or higher than the battery voltage. Measuring the system output voltage and current a maximum power point tracking (MPPT) algorithm is used to track the maximum power point of the generator, maximizing the system's efficiency. To develop the controller a linearized linear model of the converter is used alongside a dual carrier modulator to simplify the control structure. The converter behavior depends on the working points, so the controller is designed to be robust enough to control the plant in all the working conditions without achieving high bandwidth since it is used to follow the relatively slow thermal dynamics.

Thermoelectric Generator

The TEG works using the Seebeck effect's physical phenomenon, exposing some thermoelectric materials to a temperature difference ΔT they can produce an electromotive force that acts as a generator; unfortunately, these generators present a high series resistance. The characteristics of this devices are ΔT dependent and can be represented by means of linear and quadratic equations (1 - 3), where V_{oc} is the open-circuit voltage, P_{max} is the maximum power generated and R_{in} is the internal resistance of the generator, a_1 a_2 and b_1 are given constants. The typical TEG characteristics are represented in Fig. 1.

$$P_{max} = a_1 \Delta T^2 + a_2 \Delta T \tag{1}$$

$$V_{oc} = b_1 \Delta T \tag{2}$$

$$R_{in} = \frac{V_{oc}^2}{4 P_{max}} \tag{3}$$

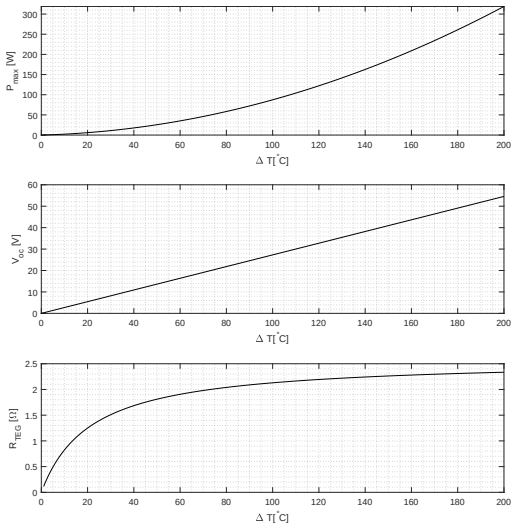

(a) Maximum Power P_{max}, Open Circuit Voltage V_{oc}, Internal Resistance R_{teg} as functions of the Temperature difference.

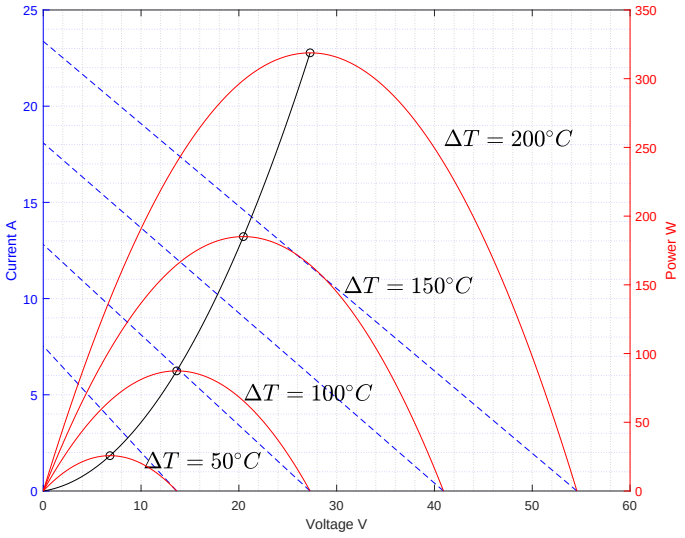

(b) Maximum Power Point in four different working conditions

Fig. 1: TEG Characteristic

Converter

As the output spans above and below 12 V a proper Non-Inverting Buck-Boost converter is used to recharge the battery system. A overall schematic of the converter is depicted in Fig. 2, where V_{in} and R_{in} is the modelled thermoelectric generator while R_{out} and V_{out} are the battery parameters. Switches T_1 and T_2 followed by the inductor can be assimilated to a buck topology. Switches T_3 and T_4, after the inductor can be assimilated to a boost topology. The buck phase is commanded by the duty cycle d_A, directly for T_1 and by the negated $\bar{d}_a$ for T_2 to avoid supply short circuit, it is also added a dead time. The boost phase is commanded by the duty cycle d_B, on T_3 and by the negated $\bar{d}_b$ on T_4, the dead time is added as for the buck phase. Accordingly to the switching frequency set to $30kHz$ the inductor value L is set to $30\mu H$ to operate in CCM. At the same time, the input and output capacitors (C_{in}, C_{out}) are obtained with the parallel of two $330\mu F$ electrolytic capacitors. The model can be expressed with a state-space representation as in (4) and (5), where the output is $y = i_{out}$, the input vector is $u = [v_{in}, v_{out}]$, the states

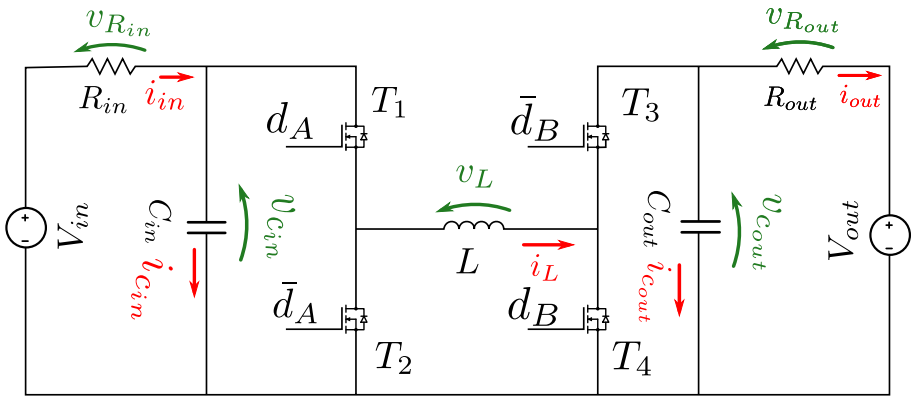

Fig. 2: Converter Schematic

vector is $x = [v_{c_{in}}, v_{c_{out}}, i_L]$ and $\dot{x}$ its derivative.

$$\dot{x} = Ax + Bu \tag{4}$$

$$y = Cx + Du \tag{5}$$

$$A = \begin{bmatrix} -\frac{1}{R_{in}C_{in}} & 0 & -\frac{d_A}{C_{in}} \\ 0 & -\frac{1}{R_{out}C_{out}} & \frac{\bar{d}_B}{C_{out}} \\ \frac{d_A}{L} & -\frac{\bar{d}_B}{L} & 0 \end{bmatrix} \tag{6}$$

$$B = \begin{bmatrix} \frac{1}{R_{in}C_{in}} & 0 \\ 0 & \frac{1}{R_{out}C_{out}} \\ 0 & 0 \end{bmatrix} \tag{7}$$

$$C = \begin{bmatrix} 0 & \frac{1}{R_{out}} & 0 \end{bmatrix} \tag{8}$$

$$D = \begin{bmatrix} 0 & -\frac{1}{R_{out}} \end{bmatrix} \tag{9}$$

Then the obtained differential equations are linearized (10 - 11) to obtain the small-signal model where the capital letters represent the DC quantities in the point in which the model is linearized. In contrast, the quantities with the "hat" are the small signals. The model built considering a non-ideal generator both as input and output produces transfer functions that are quite more accurate in describing the plant dynamics than the standard model considering only the converter [13, 14, 19] with ideal input voltage source and output load resistance.

$$\hat{i}_{out} = \frac{(1+sC_{out}ESR_{C_{out}})(C_{in}R_{in}V_{c_{in}}s + \bar{D}_B(V_{c_{in}} - D_a I_L R_{in}))\hat{d}_A}{C_{in}C_{out}LR_{out}R_{in}s^3 + L(C_{out}R_{out} + C_{in}R_{in})s^2 + R_{in}R_{out}((C_{in}\bar{D}_B^2 + C_{out}D_A^2) + L)s + (R_{in}D_A^2 + R_{out}D_B^2)} + \frac{(1+sC_{out}ESR_{C_{out}})(-C_{in}I_L LR_{in}s^2 + (C_{in}R_{in}V_{c_{out}}\bar{D}_B - I_L L)s + (-I_L R_{in}D_A^2 + V_{c_{out}}\bar{D}_B))\hat{d}_B}{C_{in}C_{out}LR_{out}R_{in}s^3 + L(C_{out}R_{out} + C_{in}R_{in})s^2 + R_{in}R_{out}((C_{in}\bar{D}_B^2 + C_{out}D_A^2) + L)s + (R_{in}D_A^2 + R_{out}D_B^2)} \tag{10}$$

$$\hat{i}_{in} = \frac{(1+sC_{in}ESR_{C_{in}})(-C_{out}I_L LR_{out}s^2 + (I_L L - C_{out}D_A R_{out}V_{c_{in}})s - I_L R_{out}\bar{D}_B - D_A V_{c_{in}})\hat{d}_A}{C_{in}C_{out}LR_{out}R_{in}s^3 + L(C_{out}R_{out} + C_{in}R_{in})s^2 + R_{in}R_{out}((C_{in}\bar{D}_B^2 + C_{out}D_A^2) + L)s + (R_{in}D_A^2 + R_{out}D_B^2)} + \frac{(1+sC_{in}ESR_{C_{in}})(-C_{out}D_A R_{out}V_{c_{out}}s + D_A(-I_L R_{out}\bar{D}_B - V_{c_{out}}))\hat{d}_B}{C_{in}C_{out}LR_{out}R_{in}s^3 + L(C_{out}R_{out} + C_{in}R_{in})s^2 + R_{in}R_{out}((C_{in}\bar{D}_B^2 + C_{out}D_A^2) + L)s + (R_{in}D_A^2 + R_{out}D_B^2)} \tag{11}$$

and the DC relations:

$$V_{c_{out}} = \frac{D_A}{\bar{D}_B} V_{c_{in}} \tag{12}$$

$$I_{in} = \frac{D_A}{\bar{D}_B} I_{out} \tag{13}$$

Control

Input Current as Controlled Output

Considering the DC gains of the output current transfer function, in buck case ($D_B = 0$, $I_L = I_{out}$):

$$\text{DC GAIN}_{\text{buck}} = \frac{\bar{D}_B(V_{c_{in}} - D_A I_L R_{in})}{R_{in}D_A^2 + R_{out}D_B^2} = \frac{V_{c_{in}} - D_A I_{out} R_{in}}{R_{in}D_A^2 + R_{out}} = \frac{V_{c_{in}} - I_{in} R_{in}}{R_{in}D_A^2 + R_{out}} \tag{14}$$

While in boost case ($D_A = 1$, $I_L = I_{in}$):

$$\text{DC GAIN}_{\text{boost}} = \frac{V_{c_{out}}\bar{D}_B - I_L R_{in} D_A^2}{R_{in}D_A^2 + R_{out}D_B^2} = \frac{V_{c_{out}}\bar{D}_B - I_{in} R_{in}}{R_{in} + R_{out}D_B^2} = \frac{V_{c_{in}} - I_{in} R_{in}}{R_{in} + R_{out}D_B^2} \tag{15}$$

In both cases, the transfer function DC gain changes sign in the point $V_{c_{in}} = I_{in}R_{in}$ or equivalently when the voltage drop across the input resistance is the same of the one delivered to the converter, that is the maximum power point making the system unstable because of the $180deg$ phase loss. This type of issue is already reported as the Middlebrook criterion [17]. For this reason, it is preferable to work controlling the converter's input current instead of the output current.

Control Structure

To reduce the two input commands (i.e. d_A, d_B) to only one (u) a dual carrier modulation is used [15, 16] in which the command signal u, namely the output of the controller, is split in the two duty cycles by comparing it with two triangular waves, that in a digital controller is equivalent to compute d_A and d_B as (16 - 22). The carrier waves used are two triangular waves W_1 and W_2 where V_{1H} and V_{1L} are the upper and lower bound of the first wave while V_{2H} and V_{2L} are the bounds for the second one, the dual carrier is set such that $V_{2H} > V_{1H} > V_{2L} > V_{1L}$ in order to create a buck-boost region and a further constraint $V_{1H} - V_{1L} = V_{2H} - V_{2L} = 1$ is added to have unity gain in control loop for both the buck and boost regions.

$$d_A = sat(K_1 u + K_2) \tag{16}$$

$$d_B = sat(K_3 u + K_4) \tag{17}$$

$$K_1 = \frac{1}{V_{1_H} - V_{1_L}} \tag{18}$$

$$K_2 = \frac{-V_{1_L}}{V_{1_H} - V_{1_L}} \tag{19}$$

$$K_3 = \frac{1}{V_{2_H} - V_{2_L}} \tag{20}$$

$$K_4 = \frac{-V_{2_L}}{V_{2_H} - V_{2_L}} \tag{21}$$

$$sat(x) = \begin{cases} 0 & \text{if} \quad x < 0 \\ x & \text{if} \quad 0 \le x \le 1 \\ 1 & \text{if} \quad x > 1 \end{cases} \tag{22}$$

The MPPT algorithm is then used to produce a reference signal for the input current of the converter I_{in}, by sensing the output current and voltage of the converter (Fig.3) in such way to maximize the

output power deliver to the battery instead of the power sourced from the generator ensuring to take into account also the efficiency given by the voltage transformation of the converter, the same approach for photovoltaic systems is used in [20]. The MPPT algorithm used is the Incremental Conductance (IC) [26] that has shown better performance with respect of P&O, other types of MPPT designed for TEG systems can be used [25, 27, 28, 29]. On the feedback branch of the measurement a low pass filter implemented with operational amplifier is placed in order to remove the output and input ripple produced by the converter. without degrading the phase of the loop.

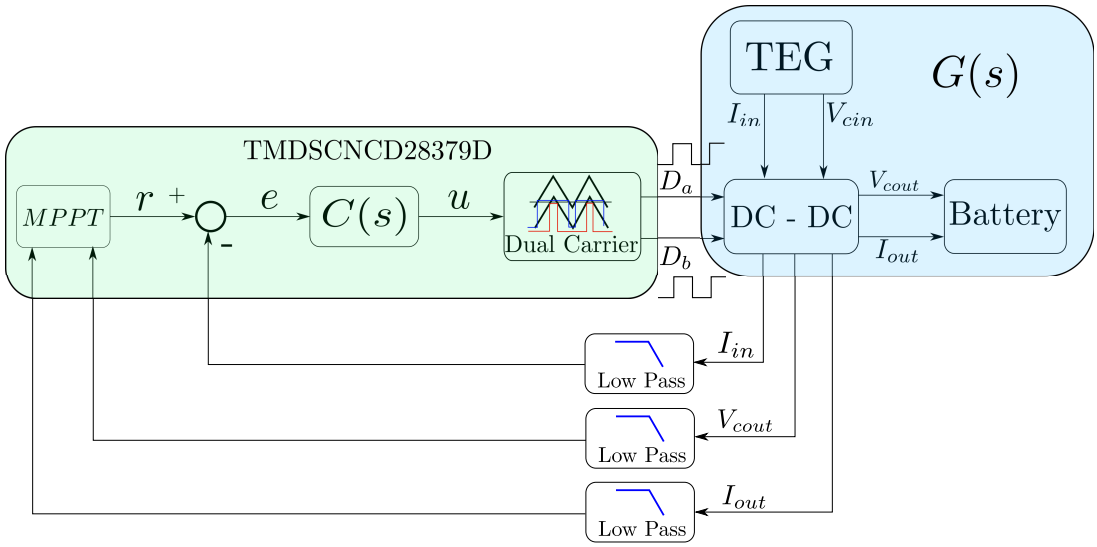

Fig. 3: Block diagram of the system

Controller Design

In Fig. 5a is showed the transfer functions of the plant $G(s)$ in the various operative conditions, as seen the steady-state gain varies with the working point as well as the second-order poles and the high-frequency dynamics introduced by ESRs. A robust loop-shaping controller is designed using weighting functions to solve mixed sensitivity optimization problem [23, 24]. An extensive set of plant working points are extrapolated considering the TEG equations to evaluate feasible working points, both in buck and boost; from this set a nominal transfer function G_n is selected (Fig. 4b), choosing one with the higher steady state gain to simplify the design of the controller $C(s)$. Some basic time domain requirements are used as reference to fix some constraints for the controller design, such as desired overshoot ($\hat{s}$) and rise time (t_r) and are converted in frequency domain requirements on the sensitivity [21], $S(s) = 1/(1+G(s)C(s))$ and complementary sensitivity, $T(s) = G(s)C(s)/(1+G(s)C(s))$, functions such as maximum magnitude (S_{max}, T_{max}) and minimum crossover frequency (ω_c) using (23) to (27).

$$\zeta = \frac{|\, ln(\hat{s})\,|}{\sqrt{\pi^2 + (ln(\hat{s}))^2}} \tag{23}$$

$$\omega_n = \frac{\pi - acos(\zeta)}{t_r\sqrt{1-\zeta^2}} \tag{24}$$

$$\omega_c = \omega_n\sqrt{\sqrt{1+4\zeta^4} - 2\zeta^2} \tag{25}$$

$$S_{max} = \sqrt{\frac{8\zeta^2 + 1 + (4\zeta^2+1)\sqrt{(8\zeta+1)}}{8\zeta^2 + 1 + (4\zeta^2-1)\sqrt{(8\zeta+1)}}} \tag{26}$$

$$T_{max} = \frac{1}{2\zeta\sqrt{1-\zeta^2}} \tag{27}$$

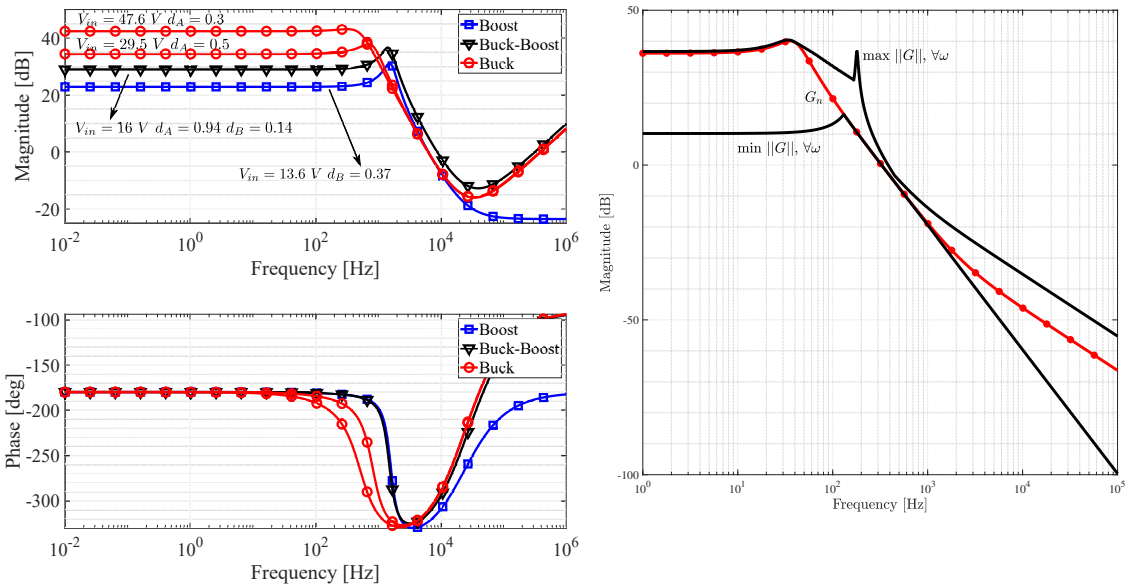

(a) Plant transfer functions $G(s)$ in four different working conditions

(b) Maximum and minimum ranges of the possible transfer functions and nominal transfer function

Fig. 4: Plant Transfer Functions

The plant uncertainties are modelled with unstructured multiplicative structure (28), the robust stability condition for this type of uncertainty is then given by (29) where $S_n(s)$ and $T_n(s)$ are the sensitivity functions computed using the nominal plant transfer function $G_n(s)$. Considering the initial set of transfer functions an additional weighting function is computed as $W_u(s)^{-1} = \max_{\forall\omega}\left(\frac{G(s)}{G_n(s)} - 1\right)$, and it is used to shape the mask for the complementary sensitivity function as $\|W_t(s)\| \leq \|W_u(s)\| \ \ \forall\omega$ accordingly to the robust stability condition (29).

$$M_G = \left\{G(s) = G_n(s)(1 + W_u^{-1}(s)\Delta s(s)) \quad , \quad \|\Delta s(s)\|_\infty \leq 1\right\} \tag{28}$$

$$\|W_u(s)^{-1} T_n(s)\|_\infty \leq 1 \tag{29}$$

With the given frequency requirements the masks for the sensitivity (30) and complementary sensitivity (31) functions are obtained. For the sensitivity function a Butterworth polynomial is used as second order denominator, a zero in the origin is added to guarantee zero tracking error, ω_2 is computed such that the maximum magnitude of the sensitivity function S_{max} that has been previously computed is respected, moreover to ensure that the sensitivity function crossover frequency is at least greater than ω_c an additional low frequency zero in ω_1 and a steady state gain c_1 as additional tunable parameter for the mask are added. For the complementary sensitivity function the same constraints are considered with the additional maximum magnitude shape introduced by $\|W_t(s)\| \leq \|W_u(s)\| \ \ \forall\omega$ (Fig. 5).

$$W_s(s) = \frac{c_1 s(1 + \frac{s}{\omega_1})}{1 + \frac{1.414}{\omega_2} s + (\frac{s}{\omega_2})^2} \tag{30}$$

$$W_t(s) = \frac{c_2(1 + \frac{s}{\omega_4})(1 + \frac{s}{\omega_4})}{(1 + \frac{s}{\omega_3})(1 + \frac{s}{\omega_3})} \tag{31}$$

Solving the optimization problem (32) the controller is designed. The computation of the controller is performed by using the "linmod()" command to obtain the generalized plant from a Simulink block diagram and "hinflmi()" to solve the optimization problem in the Matlab environment. The obtained controller is simplified by cancelling undesired high frequency dynamics until is achieved a third-order controller after some tweaking of the weight $W_1(s)$ and $W_2(s)$ starting from $W_1(s) = W_s(s)$ and $W_2(s) =$

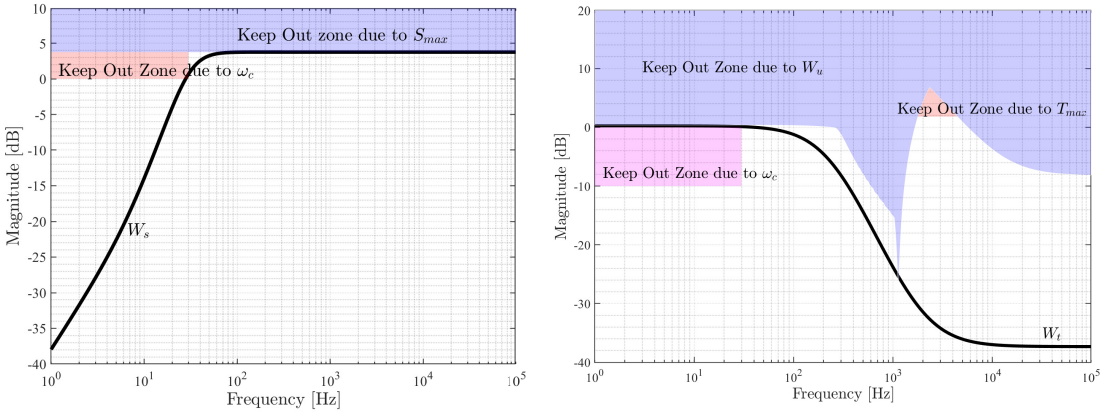

(a) W_s and its constraints

(b) W_t and its constraints

Fig. 5: Masks and Weighting functions of the sensitivity and complementary sensitivity

$W_t(s)$.

$$G_c = \arg\min_{G_c \in G_{stable}} \left(\begin{bmatrix} S_n W_1^{-1} \\ T_n W_2^{-1} \end{bmatrix} \right) \tag{32}$$

The robust stability constraint is not always met, the $W_t^{-1} T_n$ transfer function exceed $0dB$ for some points (Fig. 6) but only slightly and since the model with unstructured uncertainty is quite conservative when imposing the perturbation to compute W_u this do not represent a problem at all: as shown in (Fig. 7) the loop transfer functions with the given controller, are all stable and do not met the Nyquist point.

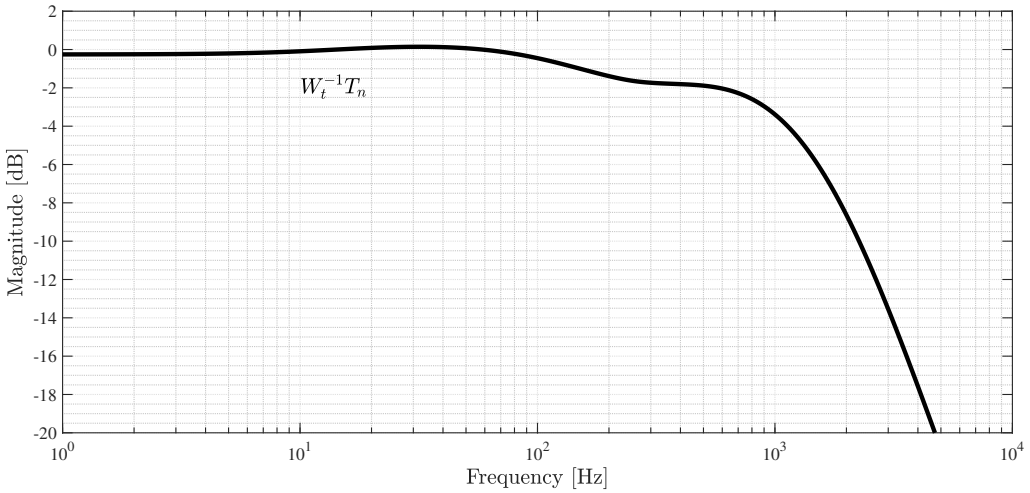

Fig. 6: Robust Stability Condition

Simulation and experimental (Fig. 8) tests, while running the same discrete controller, are performed in various points, here is reported in Fig 9, as a comparison between a simulation and experimental results, a step from $2A$ to $7A$ of input current to change also the operating condition of the converter from buck $u < V_{2L}$ to buck-boost $V_{2L} < u < V_{1H}$, recalling that $V_{2L} = -0.1$ and $V_{1H} = 0.1$; in both cases, the controller exhibits the same behavior except a slight offset in the DC value of the control variable u and input and output voltages V_{cin} and V_{cout}, these differences are imputed to the uncertainties in the input and output resistances values and the parasitic of the converter. The resulting rise time and settling time, both for experimental and simulated results, are $9.8ms$ and $40ms$ while the overshoot is 6.57%. The

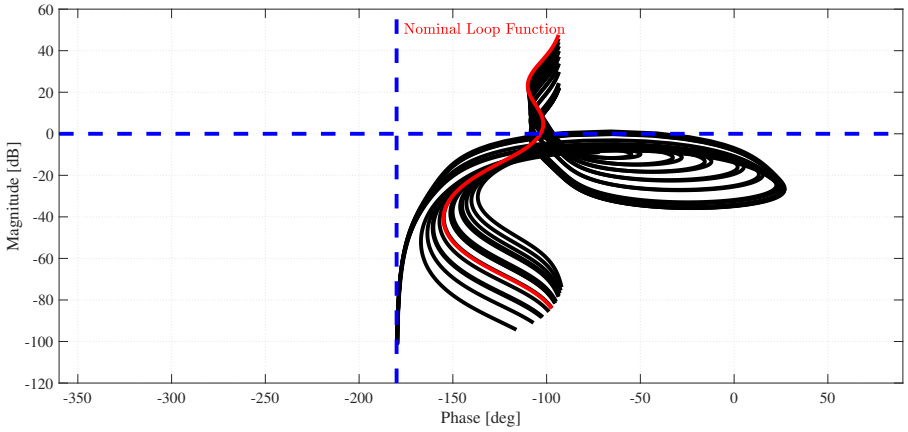

Fig. 7: Nicholas chart of the various loop functions

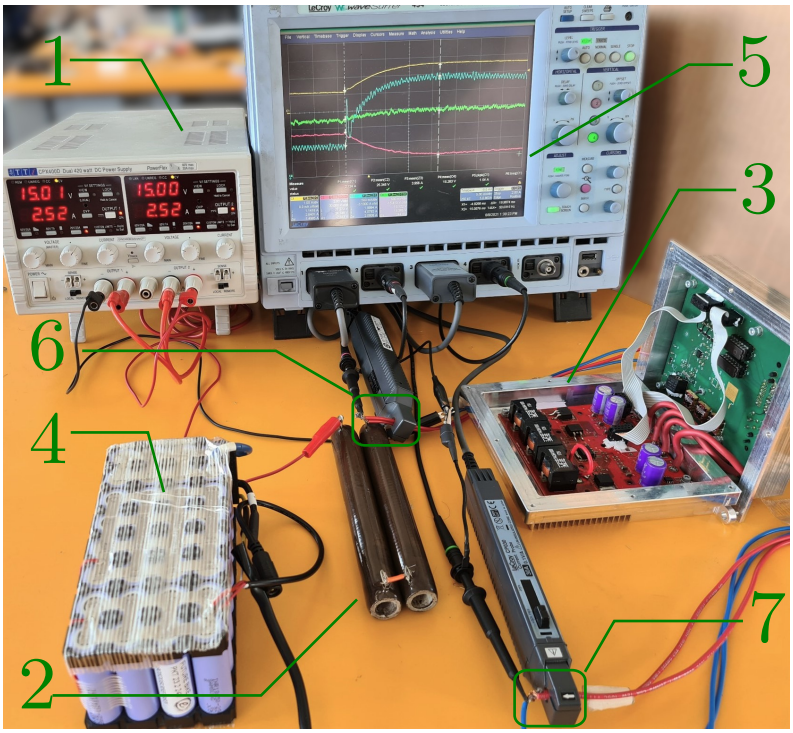

Fig. 8: Testbench: 1) Input Voltage Generator, 2) Input Resistance 2Ω, 3)Custom Non Inverting Buck Boost converter and DSP prototype, 4) Output Battery pack (8P4S with INR18650-29E cells), 5) Oscillocope Lecroy, 6) Input Measurements, 7) Output Measurements

controller is converted in discrete with a Tustin discretization for digital implementation and executed with a sampling frequency of $30Khz$ in the DSP. The MPPT must runs sufficiently slower than the given bandwidth of the system so that from one step to another, the reference change is correctly followed by the plant, for this reason the MPPT loop is implemented with a frequency of $5-15Hz$ more than enough for thermal dynamics of an exhaust system. Implementation wise the control logic is implemented in a TMS320F28379D by Texas Instruments [18].

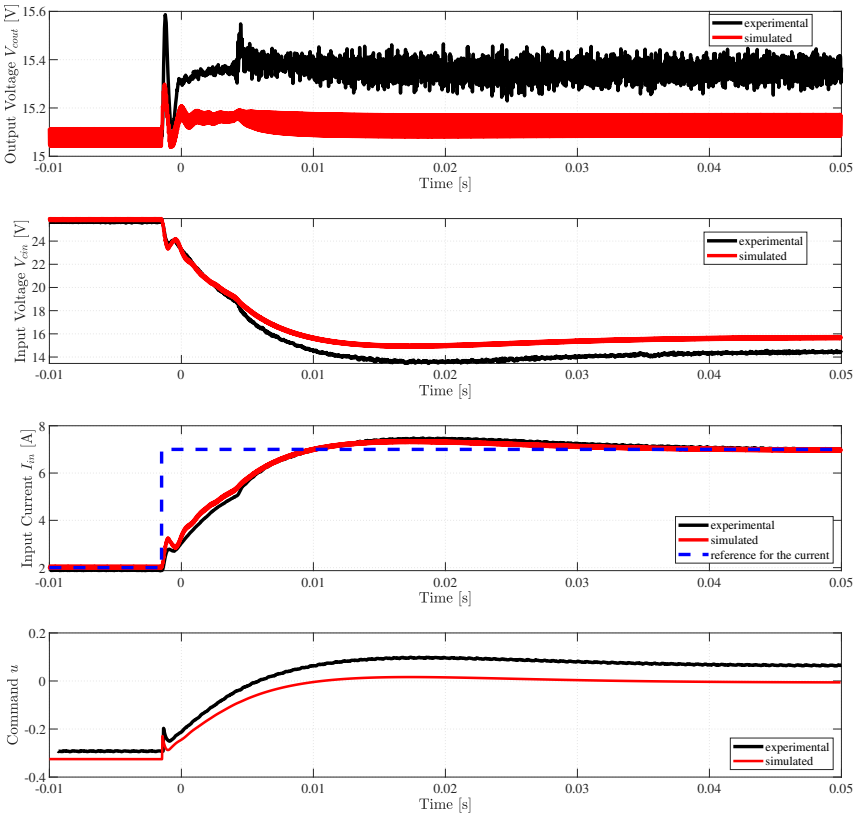

Fig. 9: Experimental And simulated results, step from 2 to 7A with an input voltage V_{in} of 30V and an input resistance of 2Ω transition from buck to buck-boost

Conclusion

The proposed converted presents high efficiency compared to other solutions in which a higher number of passive components are used, and thus the losses are inevitably higher; in our tests the efficiency obtained ranged between 0.88 to 0.96 depending on the working point and the current sourced by the TEG, even if there is always a bit of uncertainty due to efficiency measurements complexity moreover the efficiency of the system is higher when the MPPT is applied to the output of the convert. The converter non-linearity when spanning such different working conditions is another source of problems, for this reason a robust controller design is proposed that shows to be stable in all the tests performed; this type of controller suits well the given control problem especially if the bandwidth required is not too high but the working conditions can vary drastically in terms of plant transfer function's shape. To improve the boost's performance, which is reduced by the lower initial gain provided by the plant transfer function, the gain of the boost carrier can be raised by reducing the distance between V_{2h} and V_{2l} in the dual-carrier setup, increasing performance in the boost region, however a too high gain can increase the constraints given by W_t due to the resonance peak in the boost transfer functions. Simulation and experimental comparison are provided, resulting in a good match between the two, and showing the capability of the dual-carrier to be an effective way to implement a unique controller to drive both the boost and buck phases of the converter.

References

[1] Champier, Daniel : Thermoelectric generators: A review of applications, Energy Conversion and Management 2017 Vol 140, pp 167-181 2017 Elsevier

[2] Izidoro, C. L., et al. "Characterization of thermoelectric generator for energy harvesting." Measurement 106 (2017): 283-290.

[3] TWAHA, Ssennoga, et al. "Parameter analysis of thermoelectric generator/dc-dc converter system with maximum power point tracking". Energy for Sustainable Development, 2017, 41: 49-60.

[4] MOHAMED, Eid S. "Development and performance analysis of a TEG system using exhaust recovery for a light diesel vehicle with assessment of fuel economy and emissions". Applied Thermal Engineering, 2019, 147: 661-674.
[5] ALBATATI, Faisal; ATTAR, Alaa. "Analytical and Experimental Study of Thermoelectric Generator (TEG) System for Automotive Exhaust Waste Heat Recovery". Energies, 2021, 14.1: 204.
[6] PATOWARY, Rupam; BARUAH, Debendra Chandra. "Thermoelectric conversion of waste heat from IC engine-driven vehicles: A review of its application, issues, and solutions". International journal of energy research, 2018, 42.8: 2595-2614.
[7] CAO, Dong; PENG, Fang Zheng. "Multiphase multilevel modular DC–DC converter for high-current high-gain TEG application". IEEE Transactions on Industry Applications, 2011, 47.3: 1400-1408.
[8] WU, Hongfei, et al. "A TEG efficiency booster with buck–boost conversion". Journal of electronic materials, 2013, 42.7: 1737-1744.
[9] CAO, Feng, et al. "A dual-input Boost-Buck converter with coupled inductors for TEG applications". In: 2013 IEEE Energy Conversion Congress and Exposition. IEEE, 2013. p. 2020-2025.
[10] PARK, Hyunbin; SIM, Minseob; KIM, Shiho. "Achieving Maximum Power from Thermoelectric Generators with Maximum-Power-Point-Tracking Circuits Composed of a Boost-Cascaded-with-Buck Converter". Journal of Electronic Materials, 2015, 44.6: 1948-1956.
[11] CARSTENS, Jan Hendrik; GÜHMANN, Clemens. "Maximum power point controller for thermoelectric generators to support a vehicle power supply". Materials Today: Proceedings, 2015, 2.2: 790-803.
[12] KIM, Rae-Young; LAI, Jih-Sheng. "Aggregated modeling and control of a boost-buck cascade converter for maximum power point tracking of a thermoelectric generator" . In: 2008 Twenty-Third Annual IEEE Applied Power Electronics Conference and Exposition. IEEE, 2008. p. 1754-1760.
[13] Keskin, Ridvan and Aliskan, Ibrahim, "Design of Non-Inverting Buck-Boost Converter for Electronic Ballast Compatible with LED Drivers",arXiv preprint arXiv: 1907.09890, 2019
[14] Wei, Chia-Ling and Chen, Chin-Hong and Wu, Kuo-Chun and Ko, I-Ting, "Design of an average-current-mode noninverting buck–boost DC–DC converter with reduced switching and conduction losses", IEEE Transactions on Power Electronics, vol. 27, n. 12, pp 4934-4943,2012.
[15] Lee, Young-Joo and Khaligh, Alireza and Chakraborty, Arindam and Emadi, Ali, "Digital combination of buck and boost converters to control a positive buck–boost converter and improve the output transients",IEEE Transactions on Power Electronics vol. 24, n. 5, pp 1267-1279, 2009.
[16] Aharon, Ilan and Kuperman, Alon and Shmilovitz, Doron, "Analysis of dual-carrier modulator for bidirectional noninverting buck–boost converter",IEEE Transactions on Power Electronics, vol. 30, n. 2, pp=840-848, 2014.
[17] Riccobono, Antonino and Santi, Enrico, "Comprehensive review of stability criteria for DC power distribution systems", IEEE Transactions on Industry Applications, vol. 50, n. 5, pp. 3525-3535, 2014.
[18] "TMS320F2837xD Dual-Core Microcontrollers datasheet", Texas Instruments, Dallas, TX, USA. Available: www.ti.com
[19] Ma, Jianjun and Zhu, Miao and Li, Guanghui and Li, Xiuyi and Cai, Xu "Concept of unified mode control for non-inverting Buck-Boost converter", 2017 IEEE 3rd International Future Energy Electronics Conference and ECCE Asia (IFEEC 2017-ECCE Asia), pp. 1235-1240, 2017.
[20] Hester, Richard K and Thornton, Christopher and Dhople, Sairaj and Zhao, Zheng and Sridhar, Nagarajan and Freeman, Dave, "High efficiency wide load range buck/boost/bridge photovoltaic microconverter", 2011 Twenty-Sixth Annual IEEE Applied Power Electronics Conference and Exposition (APEC), pp. 309-313, 2011
[21] Karl Johan Astrom, "Control System Design", chap. 7 Specifications, 2002
[22] CERONE, V.; CANALE, M.; REGRUTO, D. "An Extended Nicholas Chart With Constant Magnitude Loci Of Sensitivity And Complementary Sensitivity Functions For Loop-Shaping Desing". IFAC Proceedings Volumes, 2006, 39.6: 547-552.
[23] KWAKERNAAK, Huibert. "Mixed sensitivity design". IFAC Proceedings Volumes, 2002, 35.1: 61-66.
[24] OUNIS, Fateh; GOLEA, Noureddine. "PID, 2-DOF PID and mixed sensitivity loop-shaping based robust voltage control of quadratic buck DC-DC converter". Advances in Electrical and Electronic Engineering, 2016, 14.5: 551-561.
[25] RODRIGUEZ, Romina, et al. "High frequency injection maximum power point tracking for thermoelectric generators". Energy Conversion and Management, 2019, 198: 111832.
[26] DOLARA, Alberto; FARANDA, R.; LEVA, Sonia. Energy comparison of seven MPPT techniques for PV systems. Journal of Electromagnetic Analysis and Applications, 2009, 2009.
[27] PARASKEVAS, Alexandros; KOUTROULIS, Eftichios. "A simple maximum power point tracker for thermoelectric generators". Energy Conversion and Management, 2016, 108: 355-365.
[28] TWAHA, Ssennoga, et al. "Performance analysis of thermoelectric generator using dc-dc converter with incremental conductance based maximum power point tracking". Energy for Sustainable Development, 2017, 37: 86-98.
[29] BIJUKUMAR, B., et al. "A linear extrapolation-based MPPT algorithm for thermoelectric generators under dynamically varying temperature conditions". IEEE Transactions on Energy Conversion, 2018, 33.4: 1641-1649.